Circadian Clock Regulation of the Secretory Pathway

Ching-Yan Chloé Yeung[1,2]¥, Richa Garva[1]¥, Adam Pickard[1], Joan Chang[1], David F. Holmes[1], Yinhui Lu[1], Venkatesh Mallikarjun[1], Joe Swift[1], Antony Adamson[1,3], Ben Calverley[1], Qing Jun Meng[1]* and Karl E. Kadler[1]*

[1] *Wellcome Centre for Cell-Matrix Research, Faculty of Biology, Medicine & Health, University of Manchester, Manchester Academic Health Science Centre, Manchester, M13 9PT UK*

[2] *Current address: Institute of Sports Medicine Copenhagen, Bispebjerg Hospital, Nielsine Nielsens Vej 11, Copenhagen NV, 2400 Denmark*

[3] *Transgenic Unit core facility, Faculty of Biology, Medicine & Health, University of Manchester, Manchester, M13 9PT UK*

¥ Authors contributed equally

* Co-corresponding authors:

KEK email: karl.kadler@manchester.ac.uk; QJM email: qing-jun.meng@manchester.ac.uk

Keywords: Circadian rhythm/Bmal1/ Collagen secretion/Protein trafficking/ER/Golgi

Proteins destined for secretion move from the endoplasmic reticulum (ER, the site of synthesis) to Golgi cisternae then to the cell surface in transport vesicles. Although the mechanism of anterograde and retrograde transport via vesicles is well understood the temporal coordination of transport between organelles has not been studied. Here we show that the extracellular levels of collagen-I (the most abundant secreted protein in vertebrates) are rhythmic over a 24-hour cycle in tendon, the tissue richest in collagen-I. Rhythmicity is the result of circadian clock control of the secretory pathway via ER-ribosome docking, Tango1-dependent ER export, phosphodiesterase-dependent Golgi-ER retrograde transport of Hsp47 (a collagen molecular chaperone), and Vps33b-dependent post Golgi export. These mechanisms pause collagen-I transport at each node of the pathway over a 24-hour cycle. Thus, the circadian clock is a master logistic operator of the secretory pathway in mammalian cells.

The cell autonomous circadian clocks are permissive time-keeping mechanisms that have evolved to optimize cellular activities in anticipation of varying demands throughout the day (*1, 2*). This temporal coordination and segregation of activities is essential to maintain the homeostasis of a given cell or tissue. Whilst the core components of the clock have been identified the downstream mechanisms that regulate cell and tissue homeostasis have remained largely unknown.

The secretory pathway contains one-third of the proteome including the protein trafficking machinery and extracellular matrix (ECM) proteins that make up 30% of the mass of vertebrates. The most abundant secreted protein is collagen, which occurs mostly as networks of fibrils that can exceed hundreds of microns in length (*3*). The fibrils provide binding sites for a wide range of macromolecules and matrix-binding integrins (*4*), making the fibrils essential for metazoan development (*5*). A homeostatic mechanism that maintains appropriate levels of collagen for tissue integrity whilst avoiding collagen excess, in the face

of changing environmental demands on cells, is implied but none has been found. Collagen excess is a hallmark of fibroproliferative diseases and numerous malignancies (*6*) but how disruption of collagen homeostasis occurs leading to fibrosis is also unknown.

We have recently identified that *Mia3* (which encodes Tango1) has a circadian rhythm in fibroblasts of tendon, a collagen I-rich tissue (*7*). Tango1 corrals CopII coats to accommodate procollagen-I (PC-I) (*8*), which has a linear length of ~300 nm and is therefore considered too large to fit into conventional 60-90 nm CopII transport vesicles (*9*). We report that secretory-pathway-specific proteins Sec61a2, Tango1, Pde4d and Vps33b, which are essential for translation and subsequent anterograde and retrograde transport and secretion of PC-I at each node in the secretory pathway, are circadian-regulated. The consequence is a daily wave of newly synthesized collagen-I protein that maintains tissue homeostasis. Mice with genetically-disrupted circadian clocks have arrhythmic expression of these proteins, as well as thickened connective tissue that is mechanically-comprised and structurally altered, thereby linking the rhythmic secretory pathway to tissue homeostasis.

Results

Circadian clock mutant mice have abnormal extracellular matrix

Tendon collagen-I fibrils are arranged in parallel register and occur as a trimodal distribution of diameters (D1 (<75 nm), D2 (75-150 nm) and D3 (>150 nm) fibrils) (Fig. 1A), which are amenable to quantitative ultrastructural study. Electron microscopy examination of the collagen fibrils in the tendons of 6-week old *ClockΔ19* mice (which have disrupted circadian rhythms (*10*) and lack a circadian rhythm in tendon (*7*)) showed a drastically different collagen fibril appearance (Fig. 1B). To selectively disrupt circadian rhythm in tendon-lineage cells a new line of Scx-Cre::*Bmal1* lox/lox knockout mice was generated and similar to ClockΔ19 mice, we identified abnormal collagen fibril profiles (Fig. 1B), diameter distribution (Fig. 1C) and profile circularity (measured as previously described (*11*)) (Fig. 1D). We confirmed circadian arrhythmia in Scx-Cre::*Bmal1* lox/lox tendons by real-time bioluminescence imaging and recording of Per2::Luc reporter, where addition of dexamethasone was able to induce a sustainable rhythm in WT tendons but not in knockout tendons (Fig. S1A, B and Supplementary Movie 1 and 2); these results are similar to *ClockΔ19* tendons (*7*), and global knockout of *Bmal1* tendons (*12*). Scx-Cre::*Bmal1* lox/lox tendons exhibited ectopic calcification at 18-weeks old which was not evident in littermate controls (data not shown). Tendons in clock-disrupted mice were significantly thicker and had reduced elastic modulus and maximum load compared to wild type littermates (Fig. S1C, D). There were no differences in fibril volume fraction between arrhythmic and wild type tendons (Fig. S1E); hence, the increased tendon width in the mutant mice was due to an increased volume of collagen. Therefore, a disrupted circadian clock results in disrupted matrix homeostasis.

Matrix organization varies during the day in wild type mice

Analysis of collagen fibril diameters of wild-type C57/BL6 mouse tendons showed rhythmic changes over the course of a day (Fig. 1E, F). Analysis of ZT3 (zeitgeber time, 3 h after lights on) and ZT15 (3 h after lights off) samples showed more circular outlines at ZT15 than at ZT3 (Fig. 1G). We found no difference in the elastic modulus of tendons at ZT3 compared to tendons at ZT15 (Fig. S1F). However, tendons isolated at ZT15 exhibited greater energy loss than tendons isolated at ZT3 (Fig. S1G, H), indicative of viscoelastic changes in the tendon during a daily cycle. These results indicated a dynamic behavior of collagen fibril organization and tissue mechanical properties that vary according to the day-night cycle.

Proteomics highlights rhythmic collagen-I synthesis

Transcriptomic profiling of tendon over 48 hours identified that collagen mRNAs were consistently arrhythmic (Fig. 1H), suggesting that the rhythmicity of extracellular collagen-I arose post-transcriptionally. Proteomic analysis of mouse tendon tissues was therefore performed (Fig. 2A). Liquid chromatography-tandem mass spectrometry (LC-MS/MS) detected ~10,000 peptides, enabling us to identify 1,474 proteins with ≥ 2 peptides per protein (Supplemental Data), with good reproducibility between biological replicates (Fig. S2). We found that approximately 10% of detected proteins (141) were robustly rhythmic (with periods of 20-27.5 hours) (Fig. 2B) with prominent changes occurring at the night-day and day-night transitions (Fig. 2B, C). The α1(I) and α2(I) chains of collagen-I were conspicuously rhythmic and levels peaked during early morning, equivalent to 1.6-fold difference in extractable collagen between day and night sampling (Fig. 2D). It was possible to identify peptides specific for the C-propeptide region of the proα1(I) chain of PC-I. This peptide peaked ~4 hours prior to the α1(I) and α2(I) peptides, consistent with the slow cleavage of PC-I to collagen-I (*10, 11*) (Fig. 2E).

To investigate the rate of collagen-I production between the diurnal phases, tendon tissues dissected 12 hours apart were labeled with ^{14}C-proline *ex vivo*. Both Achilles and tail tendon tissues (Fig. 2F and G) had significantly higher PC-I production at night, corroborating the LC-MS/MS data. ^{14}C-labeling of newly-synthesized proteins every 4 hours during 24 hours confirmed that procollagen production was ramped up throughout the night (Fig. 2H and Fig. S3A, B).

Rhythmicity in ribosome binding to ER and PC-I translation in vivo

Intrigued by the possibility that the circadian clock regulates PC-I export, we mined published databases and discovered that ribosome profiling in liver revealed circadian clock regulation of ribosome binding of the Col1a1 transcripts (*13*). The mRNAs of Col1a1 and Col1a2 (which encode α1 and α2, respectively) have a 5′ UTR consisting of 2 stems flanked by a bulge (termed the collagen 5′ stem-loop) that binds Larp6 (La ribonucleoprotein domain family member 6) and are specifically targeted to Sec61 translocons (*14*). The protein-conduction pore of the translocon is formed from Sec61α which associates with a β and a γ subunit to form a heterotrimeric complex Sec61αβγ in eukaryotes (*15-17*) (*18*). There are two *Sec61α* genes (*Sec61a1* and *Sec61a2*), which encode Sec61α; LC-MS/MS of mouse tendon only identified peptides unique to Sec61a2. Transcriptional arrays over 48 hours and analysis of proteins over 24 hours had shown that Sec61a2 was rhythmic in tendon (Fig. 3A). Western blotting showed that Sec61a2 protein was also rhythmic during 24 hours (Fig. 3B). Furthermore, electron microscopy of mouse tendon fibroblasts *in vivo* showed that the packing of ribosomes along the ER was time-of-day dependent with maxima at ZT15 (Fig. 3C, D). Therefore, expression of Sec61a2 and loading of ribosomes onto the ER in fibroblasts *in vivo* is under clock control. To determine the importance of Sec61a2 in PC-I synthesis we used CRISPR-Cas9 to knockout *Sec61a* in MEFs (Fig. S3C, D). Consequently, knockout of *Sec61a* reduced secretion of PC-I leading to fewer collagen fibres produced by *Sec61a* knockout MEFs (Fig. 3E). However, although collagen-I was translated it was not associated with the ER (Fig. 3F).

Rhythmicity in Tango1-mediated collagen export and Hsp47 retrograde traffic

PC-I has a linear length of ~300 nm and is therefore considered too large to fit into conventional 60-90 nm COPII transport vesicles (*9*) , Tango1 (encoded by the *Mia3* gene) corrals COPII coats to accommodate procollagen-I (PC-I) (*6*). In order to accommodate the increased synthesis of the bulky collagen cargo, we showed that both the transcript and protein for *Mia3*/Tango1 are also remarkably rhythmic in wild-type mice (Fig. 3G, H). There is approximately a 12-hour mismatch between the peak of transcript and protein, which might be explained by the fact that Tango1 is a 220 kDa membrane-spanning protein (*19*) in which translational delay (*20*) or ribosome stalling (*21*) might be needed to increase folding efficiency and fidelity of this multidomain protein. siRNA-mediated knockdown of *Mia3*/Tango1 (Fig. S3E, F) in synchronized

MEFs resulted in co-localization of protein disulfide isomerase (PDI, an ER marker) and PC-I with decreased levels of extracellular fibrillar collagen (Fig. 3I).

Tango1 binds Hsp47 (*22*) to direct PC-I into large-diameter ER exits (*19*). Hsp47 is an ER-resident molecular chaperone required for the formation of a stable triple helix and is essential for normal development in mice (*23*). Unlike other molecular chaperones, Hsp47 specifically recognizes the folded conformation (the triple helix) of its client (*24, 25*). Hsp47 contains an ER retrieval sequence, which on arrival at the cis-Golgi, presumably leads to activation of the Kdel receptor (Kdelr). Activation of the Kdelr in other systems has been shown to trigger a cascade involving phosphodiesterase (Pde) inhibition of protein kinase A (Pka) and phosphorylation of transport machinery to maintain homeostasis of signaling and transcriptional networks (*26*). Pde7a1 via Pka is known to regulate retrograde transport of the Kdelr (*26*). However, Pde7a1 did not appear to be rhythmic at the transcript or protein levels in tendon. We noticed that Pde4d was rhythmically expressed at the transcript and protein levels (Fig. 3J, K) in mouse tendon; therefore, we suspected that Pde4d might be required for retrograde transport of Hsp47. We co-localized Gm130 (an ERGIC and cis-Golgi marker) and Hsp47 in synchronized MEFs. We observed maximal co-localization at 19 hours post synchronization (Fig. 3L), which coincided with the peak of Pde4d expression in synchronized MEFs (not shown). We used siRNA to knockdown Pde4d expression or Cdp840 to inhibit Pde4 activity (Fig. S3G, H). Both treatments caused intracellular retention of PC-I (Fig. S3I). Diminished Pde4d expression caused accumulation of Hsp47 in the cis-Golgi (Fig. 3M) and inhibited PC-I secretion in Cdp840-treated MEFs (Fig. S3I, J). There was also an increased association of Hsp47 and collagen I in Cdp840-treated MEFs (Fig. 3N). Hsp47 is a collagen-specific molecular chaperone; consequently, fibronectin is not colocalized with Hsp47, and inhibition of Pde4d by Cdp840 had no effect on the formation of fibronectin fibres (Fig. S3K).

Vps33b post Golgi transport is rhythmic and essential for PC-I secretion

The requirements for PC-I posttranslational modification in post-Golgi compartments are less understood but recent studies suggest a role for Vipar in the regulation of lysyl hydroxylation by Plod3 (procollagen-lysine,2-oxoglutarate 5-dioxygenase 3) in collagen IV (*27*). The transcript for Vps33b, a binding partner of Vipar, as well as the Vps33b protein, are rhythmic in tendon, peaking at the end of the circadian cycle (Fig. 4A, B). CRISPR-Cas9 mediated knockout of *Vps33b* (Fig. S3L, M, N) greatly diminished the assembly of collagen fibres in later time points when Vps33b reaches maximal expression (Fig. 4C). Strikingly, *Vps33b* KO clones were unable to produce long collagen fibrils (Fig. S4). The intracellular collagen in *Vps33b* KO cells co-localizes with the ER marker, Pdi, suggesting it has been retained in the ER (Fig. S4). Interestingly, in later time points, when levels diminish in the ER, there is an increased localization with the cis-Golgi (Fig. 4C). Also, the distribution of collagen-I had a vesicular appearance (Fig. S4), which might indicate that the previously retained PC-I was being turned over intracellularly. In a final experiment, we showed that the transcripts for Sec61a2, *Mia3*, Pde4d and Vps33b are disrupted in *Clock∆19* mice (Fig. 4D, E), consistent with an abnormal matrix in these mice.

Discussion

Our findings define a new role for the circadian clock in regulating the timing of membrane and protein traffic throughout the secretory pathway for connective tissue homeostasis. We found that levels of extractable collagen-I oscillate during 24 hours. The transcript levels of collagen-I polypeptide chains (and those of other fibril-forming collagens) were not rhythmic; therefore, the rhythmicity of extracellular collagen-I arises post-transcriptionally. We went on to show that the rhythmicity of extracellular collagen-I is generated in the secretory pathway via ribosome binding, Sec61a2-dependent PC-I translation, Tango1-dependent ER export, Pde4d-dependent retrograde traffic of Hsp47, and Vsp33b-dependent post-Golgi

transport. As discussed by Cancino et al., (*26*), a fundamental property of cells is to maintain homeostasis between ER and Golgi membranes. This ability must extend throughout the secretory pathway where specific machinery must exist at each node in the pathway to ensure integration of signaling pathways and feedback loops. Our data show that the circadian clock acts as a "conductor" to temporally coordinate protein and membrane transport across all nodes in the pathway.

Much of what we currently understand about connective tissue homeostasis comes from studies of collagen's slow turnover, where the half-life can exceed the life expectancy of the animal (*28-32*). However, the fact that the fibrils persist a lifetime in heavy-loaded tissues such as tendon poses a conundrum: how do the fibrils resist failure fatigue despite daily variations in loading regimes, countless cycles of loading and unloading at levels that would destroy isolated cells, all in the face of no renewal?

The difficulty with the zero turnover model is that fibroblasts in tissues with a slow collagen turnover, such as tendon, show evidence of collagen synthesis (*33, 34*) in response to mechanical and hormonal stimuli (*35-37*). Furthermore, microdialysis of human Achilles tendon show elevated levels of the C-propeptides of PC-I after moderate exercise (*38, 39*), which is direct evidence for the ability of tendon fibroblasts to synthesize collagen in vivo. These observations led to an alternative hypothesis in which a pool of collagen is produced and removed on a daily basis, and which has escaped detection in studies of collagen turnover. Support for this hypothesis comes from observations of a circadian rhythm in the serum concentration of type I procollagen N- and C-propeptides (*40, 41*) and the circadian rhythm of bone collagen degradation products (*42*). However, evidence for this model has been restricted to physiological and clinical observations. Here, we show that levels of extractable collagen-I are diurnally rhythmic, ^{14}C-proline labeling shows PC-I synthesis predominately at night, and PC-I enters and exits the secretory pathway on a 24-hourly cycle. Sec61, Tango1, Pde4d and Vps33b are each essential for PC-I transport and the protein levels are rhythmic and sequential. Therefore, the transport of PC-I through the secretory pathway is stepwise and regulated at each node (see schematic in Fig. 4F). It is possible that the levels of each of these proteins could fall to zero as a mechanism to pause the export of PC-I from any particular node in response to external influences or the need to achieve particular post-translational modifications of PC-I, including conversion to collagen-I. Conversely, rhythmicity could be removed and levels of these proteins could rise to facilitate rapid export of PC-I, to facilitate rapid matrix formation.

In this study we did not explore the mechanism of collagen fibril turnover. The homeostasis of collagen-I levels in the face of rhythmic secretion of collagen-I implies a corresponding mechanism of collagen removal, which could also exhibit rhythmicity. Biochemical pathways have been identified that combine extracellular matrix metalloproteinases (MMPs) and intracellular lysosomal proteinases, respectively (*43*). Peptides arising from cathepsin K were rhythmic in the LC-MS/MS proteomics analysis (Supplementary Data). Cathepsin K is a lysosomal proteinase found in osteoclasts and fibroblasts that can degrade collagen (*44*). It is also possible that collagen turnover could involve mechanical damage to the molecule followed by degradation by non-specific proteinases.

The rhythmic changes in collagen-I levels in wild-type mice were in line with diurnal changes in the distribution of collagen fibril diameters and roughness of fibril surfaces. There has been poor agreement on the precise diameters of collagen fibrils, and on the occurrence of a unimodal, bimodal or trimodal distribution of diameters in tissues. We suggest that the discrepancies might have arisen, in part, because of time of day sampling. A further misunderstanding has been the circularity (roughness) of fibril cross sections. It has been generally assumed that fibrils are smooth cylinders. However, we showed that the fibrils have rough surfaces, and that the deviation from circularity is time of day dependent. The diurnal changes in fibril circularity and roughness, combined with the diurnal variation in collagen-I levels and synthesis, are indicative of a homeostatic chronomatrix that is sacrificial and replaced daily. The identification of the molecular mechanisms governing collagen homeostasis, highlighted in this paper, has

large implications for our understanding of disease mechanisms in fibrosis and cancer, and in aging, which are all associated with matrix dysregulation.

Materials and Methods and Supplementary Information

Ethics

The care and use of all mice in this study was carried out in accordance with the UK Home Office regulations, UK Animals (Scientific Procedures) Act of 1986 under the Home Office licence (#70/8858 or I045CA465). The permission included the generation of conditional knock out animals.

Mice

ClockΔ19 mice (C57BL/6 on a *Per2*::Luciferase reporter background) were as described previously (*10*). To generate mice in which Bmal1 is ablated in tendon-lineage cells, we crossed mice expressing Cre recombinase under the control of the Scleraxis promoter (Scx-Cre; C57BL/6) (*45*) with C57BL/6 mice carrying loxP sites flanking the exon encoding the BMAL1 basic helix-loop-helix domain (*46*) bred on a background with *Per2*::Luciferase reporter (*47*) to produce Scx-Cre:*Bmal1* lox/lox mice. Six-week old wild type C57BL/6 mice housed in 12-h dark/12-h dark cycle (DD) were used for circadian time (CT) time-series microarray and protein extraction for western blotting as previously described (*7*). Wild type C57BL/6 mice housed in 12-h light/12-h dark cycle (LD) were used for zeitgeber time (ZT) studies of time-dependent qPCR analyses, mechanical testing, ultrastructural analyses and proteomics.

Luminometry

Tendon explants from 6-week old mice were cultured on 0.4 μm cell culture inserts (Millipore) in recording media (containing 0.1 mM Luciferin) in the presence of 100 nM dexamethasone and visualized using a self-contained Olympus Luminoview LV200 microscope (Olympus) and recorded using a cooled Hamamatsu ImageEM C9100-13 EM-CCD camera. Images were taken every hour for 3 days, and combined in ImageJ to generate movies. The recording parameters were the same for control wild type and Scx-Cre:*Bmal1* lox/lox Achilles tendons but the brightness for the Scx-Cre:*Bmal1* KO recording was increased for the images and video to enable visualisation. LumiCycle apparatus (Actimetrics) was used for real-time quantitative bioluminescence recording of tendon explants prepared as described above in the absence of dexamethasone for 3 days. Then 100 nM dexamethasone was added to re-initiate the circadian rhythms. Baseline subtraction was carried out using a 24-hr moving average. Period after addition of dexamethasone was calculated using LumiCycle analysis software (Actimetrics) or using the RAP algorithm. A minimum of three peaks were used to determine period. Amplitude was calculated as peak-trough difference in bioluminescence of the second peak using base-line subtracted data.

Mechanical testing

Mechanical properties of arrhythmic tendons were measured as described previously (*48*). In brief, tail tendons were dissected from 6-week-old mice and mounted onto a (grade 100) sandpaper frame with a 1 cm length window using superglue. The sandpaper frame was clamped in an Instron 5943 fitted with a 100 N load cell (Instron Inc, UK). Only samples that failed in the mid portion of the tendon were included. Tendons were tested to failure with a strain rate of 5 mm/min. The length and width of the samples tested were measured from a digital photograph using ImageJ software, which were used to derive corrected elastic modulus and calculate maximum load/cross sectional area. At least 10 tendons from each biological replicate were tested. The dissected mouse Achilles tendons sampled at different times of the day were

subjected to a cyclic test regime on an Instron 5943 fitted with a BioPuls specimen bath. Each sample was clamped at the bone and over the myotendinous junction using superglue and a sandpaper sandwich in the pneumatic clamps. The sample bath was filled with PBS and maintained at 22°C. The tendon was straightened with a tare load of 0.02 N and then subjected to successive strain cycles up to a 1 N load. A series of 30 cycles was used for each tendon sample and consisted of 6 sets of 5 cycles with a strain rate for each set of 1, 2, 3, 4, 5 and 1 mm/min, respectively. The tendon was finally loaded to 1 N at 1 mm/min after the last strain cycle and the stress-relaxation load curve was recorded over 15 min. Energy loss measurements were obtained from the stress-strain hysteresis loop of the final cycle in each set. The elastic modulus was calculated from the linear part of the stress-strain curve on the load increasing part of the strain cycle. The length of the test portion of the tendon and the lateral dimensions were measured from calibrated images. The stress-relaxation curve was fitted to a sum of three exponential decay curves of to yield 3 characteristic relaxation times (T_1, T_2, T_3).

Electron microscopy and morphometric analyses

Tendons from 5- to 6-week old mice were prepared for transmission electron microscopy (TEM) and serial block face-scanning electron microscopy (SBF-SEM) were prepares as described previously (*11*). Fibril diameter, perimeter and area were measured using ImageJ software to calculate circularity and fibril volume fraction as described previously (*11*). Fibril diameter distributions were plotted and fitted to 3-Gaussian distribution using Sigma Plot 12.0 software (Systat Software) as previously described (*11*).

Mass spectrometry

All reagents were of mass spectrometry grade. Tail tendons were homogenized with a bullet blender (with 1.6 mm steel beads; Next Advance) at maximum speed at 4 °C for 5 min in 200 µL of SL-DOC buffer (1.1% SL (sodium laurate), 0.3% DOC (sodium deoxycholate), 0.5 mM dithiothreitol (DTT) in 25 mM AB (ammonium bicarbonate)), supplemented with protease and phosphatase inhibitor cocktails (Roche). Samples were incubated at 4 °C for 5 min, alkylated with 12 µL of 30 mM of IAM (iodoacetamide) for 20 min at RT, followed by quenching with 12 µL of 30 mM DTT. Samples were centrifuged at maximum speed for 10 min. Supernatants were transferred into LoBind tubes (Eppendorf) and protein concentrations measured using a Millipore Direct Detect spectrometer. A total of 2 µg protein per sample was digested using trypsin beads (SMART digestion kit, Thermo Scientific) with rapid agitation (1400 rpm) at 37 °C overnight. Peptide/bead mixtures were centrifuged at 12000 g for 5 min and supernatants transferred into new tubes. The pH was adjusted to < 3 by addition of 10% FA (formic acid, Sigma Aldrich) and 400 µL of EA (ethylacetate, Sigma Aldrich). Samples were then spun for 5 min at 16000 g, and the upper layer of solvent (EA) was discarded. EA extraction was repeated twice and samples were lyophilized in a speed-vac centrifuge (Heto). Samples were desalted, in accordance with the manufacturer's protocol, using POROS R3 beads (Thermo Fisher) and lyophilized. The resulting peptides were dissolved in 15 µL of 5% acetonitrile with 0.1% formic acid.

Digested samples were analyzed using an UltiMate® 3000 Rapid Separation liquid chromatography system (RSLC, Dionex Corporation) coupled to either an Orbitrap Elite (for quality control assessment; Thermo Fisher Scientific) or Q Exactive HF (Thermo Fisher Scientific) mass spectrometer. Briefly, for the Orbitrap Elite, peptides were separated using a 75 mm x 250 µm inner diameter 1.7 µM CSH C18, analytical column (Waters) with a gradient from 92% A (0.1% formic acid, FA, Sigma, in deionized water) and 8% B (0.1% FA in acetonitrile) to 33% B, in 104 min at 300 nL/min. For the Q Exactive HF, peptides were separated in a gradient of 95% A and 5% B to 7% B at 1 min, 18% B at 58 min, 27% B in 72 min and 60% B at 74 min at 300 nL/min using a 75 mm x 250 µm inner diameter 1.7 µM CSH C18, analytical column (Waters). Peptides were selected for fragmentation automatically by data dependent analysis.

Proteomics data analysis and protein quantification

Spectra from multiple samples were automatically aligned using Progenesis QI (Nonlinear Dynamics) with manual placement of vectors where necessary. Peak-picking sensitivity was set to 4/5 and all other parameters were left as defaults. Only peptides with charge between +1 to +4, with 2 or more isotopes were taken for further analysis. Filtered peptides were identified using Mascot (Matrix Science UK), by searching against the SwissProt and TREMBL mouse databases. The peptide database was modified to search for alkylated cysteine residues (monoisotopic mass change, 57.021 Da), oxidized methionine (15.995 Da), hydroxylation of asparagine, aspartic acid, proline or lysine (15.995 Da) and phosphorylation of serine, tyrosine, threonine, histidine or aspartate (79.966 Da). A maximum of 2 missed cleavages was allowed. Peptide detection intensities were exported from Progenesis QI as Excel (Microsoft) spread sheets for further processing. Peptide identifications were filtered via Mascot scores so that only those with a Benjamini-Hochberg false discovery rate (FDR)-adjusted p-value < 0.05 remained. FDR filtering was performed as described in (*49*). Raw ion intensities from peptides belonging to proteins with fewer than 2 unique peptides (by sequence) per protein in the dataset were excluded from quantification. Remaining intensities were logged and normalized per MS run by the median logged peptide intensity. Peptides assigned to different isoforms were grouped into a single "protein group" by gene name. Only peptides observed in at least 2 samples were used in quantification. Missing values were assumed as missing due to low abundance, an assumption others have shown is justified (*50*). Imputation was performed at the peptide level following normalization using a method similar to that employed by Perseus (*51*) whereby missing values were imputed randomly from a normal distribution centered on the apparent limit of detection for this experiment. The limit of detection in this instance was determined by taking the mean of all minimum logged peptide intensities and down-shifting it by 1.6σ, where σ is the standard deviation of minimum logged peptide intensities. The width of this normal distribution was set to 0.3σ as described in (*51*). Fold-change differences in the quantity of proteins detected in different time-points were calculated by fitting a mixed-effects linear regression model for each protein with Huber weighting of residuals (*52*) as described in (*50*) using the fitglme Matlab (The MathWorks, USA) function with the formula:

$$y_{iptb} = \beta_t + \beta_p + \beta_b$$

Where y_{iptb} represents the $\log_2$(intensity) of peptide *p* belonging to protein i, at time-point *t*, in batch *b*. βs represents effect sizes for the indicated coefficients. *Batch* and *peptide* were entered as random effects whereas *time-point* was entered as a fixed effect. Standard error estimates were adjusted with Empirical Bayes variance correction according to (*53, 54*). Conditions were compared with Student's t-tests with Benjamini-Hochberg correction for false positives (*55*).

Periodicity analysis

Periodicity analysis was performed using the MetaCycle package (*56*) in the R computing environment (*57*) using the default parameters. A Benjamini-Hochberg FDR<0.2 was used to detect rhythmic proteins.

^{14}C-proline labeling of tendons *ex vivo*

Tendons were dissected from mice, rinsed in PBS, and incubated at 37°C in 2.5 Ci/ml of ^{14}C-proline for one hour, with the tubes agitated every 20 min. After incubation, tissues were washed, spun down and transferred to fresh Eppendorf tubes with 100µl of salt extraction buffer (1 M NaCl, 25 mM EDTA, 50 mM Tris-HCl, pH7.4) containing protease inhibitors and phosphatase inhibitors. Tendons were extracted in 2 changes of salt extraction buffer – 12 hours (S1), 6 hours (S2) – these steps extracted collagen that was present in the extracellular fraction of the tissue. This was then followed by 12 hours in NP40 buffer (salt

extraction buffer supplemented with 1% NP40) which allowed extraction of intracellular fractions. NP40 extracts were then analyzed on 6% Tris-Glycine gels (Invitrogen) under reducing conditions, followed by transfer onto nitrocellulose membranes. Membranes were then dried and exposed to a phosphoimaging plate (Fuji BAS-III or BAS-MS). After 14 days of exposure, the plates were processed using a phosphoimager (Fuji BAS 2000 or 1800), and images analyzed using ImageJ.

Cell culture

Tail tendon fibroblasts were released from 6-8 week mouse tail tendons by 1000 U/ml bacterial collagenase type 4 (Worthington Biochemical Corporation) in trypsin (2.5 g/l) as previously described (*58*) and immortalized by retroviral expression of mTERT (iTTF) (*59*). Mouse embryonic fibroblasts were isolated from E14 wild type mouse embryos. Cells were cultured in complete media (Dulbecco's modified Eagle's medium: Nutrient Mixture F-12 containing 4500 mg/L glucose, L-glutamine, and sodium bicarbonate, supplemented with 10% fetal calf serum) at 37°C, in 5% CO_2. To synchronize the circadian clocks of a population of cells, cells were incubated with 50% horse serum in complete media for 2 h at 37°C, in 5% CO_2 and then for 24 h in complete medium at 37°C, in 5% CO_2. After (at 0 h after synchronization), cells were fixed for immunofluorescence or used for protein or RNA isolation, at 3-h or 4-h intervals.

Gene knockout by CRISPR-Cas9 and gene knockdown by siRNA

Cells were treated with CRISPR-Cas9 to delete *Sec61a1*, *Sec61a2* or *Vsp33b* genes. Ribonucleoprotein complexes of crRNA, tracrRNA and recombinant 3xNLS Cas9 were formed according to manufacturer's protocol (Integrated DNA Technologies). Two different guides were used in combination to target *Sec61a1* (g1: TCCGGCAAGATGACACAGAA, g2: TCTGCAAAAAGGGTACGGCT), *Sec61a2* (g1: AGTTTAGAGAGAAGGTACTA, g2: TTTATGATCGCTCACATTTC) or *Vps33b* (g1: CGTTAGCAATTCGATCCAAA, g2 AGTCATCCTAAGCCCTCAGA). 60 pmol complexes (2 pmol Cas9) were nucleofected into 4 x 10^5 MEFs using P1 Nucleofection Buffer (Lonza). Cells were treated with siRNAs to deplete *Mia3* or *Pde4d* transcripts. siRNAs targeting *Pde4d* (SMARTpool: ON-TARGETplus Pde4d siRNA; GE Healthcare) or *Mia3* were transfected into MEFs using MEFs Nucleofector Kit (Lonza) according to the manufacturer's instructions. Briefly, 4 x 10^6 cells (in a well of a 6-well plate) were transfected with a 0.8 nmol of siRNA in a final volume of 3 mL (yielding a final concentration of 250 nM). For iTTF studies, 5 x 10^4 cells were plated out in a 24-well plate, and the aforementioned ribonucleoprotein complexes were introduced into the culture using Lipofectamine® RNAiMAX reagent (Thermofisher), according to manufacturer's instructions. Clones were then generated using serial dilution in a 96-well plate. Gene knockout and knockdown was confirmed by western blotting and qPCR.

Immunofluorescence

Cells were fixed with 100% methanol at -20 °C and permeabilized with 0.5% Triton-X/PBS. Collagen-I was detected using a rabbit pAb (1:500; OARA02579, Gentaur), Hsp47 was detected using mouse mAb (1:100; sc-398579, Santa Cruz), ER was detected using rabbit pAb to Calnexin (1:200; ab75801, Abcam) or mouse mAb protein disulfide isomerase (Pdi) (1:100; ab190883, Abcam), cis-Golgi was detected using rabbit mAb to Gm130 (1:250; ab67391, Abcam) or mouse pAb to Gm130 (1:500; 610822, BD Biosciences), Sec61a was detected using a rabbit pAb (1:50; sc-12322, Santa Cruz) and fibronectin was detected using a mouse mAb (1:200, ab6328, Abcam). Images were collected on a Leica TCS SP5 AOBS inverted confocal using a [60x / 0.50 Plan Fluotar] objective [and 3x confocal zoom]. The confocal settings were as follows, pinhole [1 airy unit], scan speed [1000Hz unidirectional], format 1024 x 1024. Images were collected using [PMT] detectors with the following detection mirror settings; [FITC 494-530 nm; Cy5 640-690 nm] using the [488 nm (20%), 594 nm (100%) and 633 nm (100%)] laser lines respectively. To eliminate crosstalk between

channels, the images were collected sequentially. When acquiring 3D optical stacks the confocal software was used to determine the optimal number of Z sections. Only the maximum intensity projections of these 3D stacks are shown in the results.

Polymerase chain reaction

For qPCR analysis, the $2^{-\Delta\Delta Ct}$ method (*60*) was used to analyze relative fold changes in gene expression compared to the first time point or to wild type or control. Primer sequences used were *Mia3* AGC CAC GGA CGG CGT TTC TC and CCC CTG CCA GTT TGT AGT A, *Gapdh* AAC TTT GGC ATT GTG GAA GG and ACA CAT TGG GGG TAG GAA CA, *Pd4de* CCA ACT AGC CTC CCC TTG AA and GCT GTC AGA TCG GTA CAG GA, *Sec61a1* CAG GTT CTT CTG CCA AAG ATG and TCA TGC ACC ATG GAG GTC T, *Sec61a2* TGT ATG TCA TGA CGG GGA TG and CAA ACC AGC AAC AAA CAA CTG and *Vps33b* GCA TTC ACA GAC ACG GCT AAG and ACA CCA CCA AGA TGA GGC G.

Western blotting

Protein was extracted and analyzed by western blotting as previously described (*7*). Primary antibodies used were rabbit pAb to Tango1 (1:500; H-156, Santa Cruz), mouse mAb to Gapdh (1:10000; clone Gapdh-71.1, Sigma), rabbit pAb to Pde4d4 (1:500; antibody shows cross reaction to Pde4d1 and Pde4d3), goat pAb to collagen α1 type I (1:1000; sc-8784, Santa Cruz), rabbit pAb to Sec61A (1:500; sc-12322, Santa Cruz), mouse mAb to vinculin (1:200, CP74, Oncogene), and mouse mAb to Vps33b (1:500, G-9: sc-398322, Santa Cruz).

Acknowledgements

The research was funded by generous grants from Wellcome (110126/Z/15/Z and 203128/Z/16/Z), MRC (MR/P010709/1) and Arthritis Research UK (20875). VM was supported by a studentship from the Sir Richard Stapley Educational Trust. JS was funded by a Biotechnology and Biological Sciences Research Council (BBSRC) David Phillips Fellowship (BB/L024551/1). The authors would like to thank Ronen Schweitzer (Shriners Hospital for Children, Portland, OR, USA) for Scx-Cre mice, Alison Hallworth and Raymond Hodgkiss and the University of Manchester Biological Support Facility for assistance in animal welfare and husbandry, and Michal Dudek and Nan Yang (University of Manchester) for assistance with bioluminescence imaging. The proteomics was performed at the Wellcome Centre for Cell-Matrix Research Proteomics Core Facility, and the electron microscopy was performed in the Electron Microscope Suite, Faculty of Biology, Medicine and Health, University of Manchester.

Author contributions:

C-YCY and RG designed and performed experiments, interpreted data and drafted the manuscript. AP, JC, DFH, YL and BC designed and performed experiments and interpreted data. VM, JS and AA contributed materials and analysis tools. Q-JM and KEK conceived the project, supervised the experiments and wrote the manuscript.

Figure legends

Figure 1. Circadian regulation of the collagen extracellular matrix

(A) Trimodal distribution of fibril diameters D1 (<75 nm), D2 (75-150 nm) and D3 (>150 nm). **(B)** Representative transverse transmission electron microscopy images of tail tendons from 6 week-old wild type, *ClockΔ19* and Scx-Cre:*Bmal1* lox/lox mice showing irregular fibril cross sections in mutant tendons. Bars 200 nm. **(C)** Fibril diameter distributions measured from transverse TEM images of wild type,

*Clock*Δ*19* and Scx-Cre:*Bmal1* lox/lox tail tendons showing abnormal distribution of fibril diameters and increase in large (>400-nm fibrils) in mutant tendons (>1000 fibrils measured). Red lines show 3-Gaussian fit curves. **(D)** Circularity of D1, D2 and D3 collagen fibrils of tail tendons sampled from *Clock*Δ*19* and Scx-Cre:*Bmal1* lox/lox mice and their wild type litter mate controls (192 wild type fibrils and 179 *Clock*Δ*19* fibrils measured. 664 wild type fibrils and 506 Scx-Cre:*Bmal1* lox/lox fibrils measured; ***$p<0.0001$ in D1, D2 and D3 populations in mutants compared to same populations in littermate controls). The circularity of fibrils from global *Clock*Δ*19* tendons being more irregular than fibrils from Scx-Cre:*Bmal1* lox/lox is likely due to due to a residual circadian rhythm from cells that were not derived from Scleraxis-lineage cells. **(E)** Transverse TEM images of Achilles tendon at ZT3 and ZT15. Bars 200 nm. **(F)** Fibril diameter distributions measured from images of transverse TEM images of Achilles tendon at ZT3 and ZT15 show a shift in collagen fibril diameter distribution (>1000 fibrils measured). **(G)** Circularity of collagen fibrils examined in transverse TEM images of Achilles tendons from ZT3 and ZT15 indicate fibril cross sections from ZT3 are more irregular than fibril cross sections from ZT15 (914 ZT3 fibrils and 948 ZT15 fibrils measured; ***$p<0.001$). **(H)** Expression of collagen genes in wild type mouse tail tendon tissue detected by different probe sets in a time series microarray study were not rhythmic (n=2). Grey shadow indicates subjective night phase. Error bars show SEM.

Figure 2. Time-series proteomics analysis of proteins in mouse tendon

(A) Schematic showing collection of mouse tail tendons every 4 h during 48 h for proteomics analysis. **(B)** Heat map depicting the levels of the detected rhythmic proteins, organized according to the timing of peak expression in zeitgeber time (ZT) (n=4). Red is down-regulated and blue is up-regulated based on protein Z-score. **(C)** Radial plot showing the frequency distribution of the phases of the rhythmic proteome in mouse tendons. The majority of peptides were detected between ZT6-9 and ZT17-19. **(D)** Relative abundance of the two collagen-I α chains, α1(Col1a1) and α2(Col1a2), detected by mass spectrometry during 48 h (mean of log10 intensities for n=4, ±SEM). Peak abundance of collagen-I peptides was detected at ZT27 and ZT47. **(E)** Peptide counts (log_2 values) of C-propeptide region of α1(Pro-Col1a1) chain and of α1(Col1a1) detected by mass spectrometry during 48 h, based on calculations using peptides from the different sub-domains of pro-α1(I) chain. Note the abundance of C-pro-α(1) peptides peaks prior to the peak abundance of α1(I) peptides, at ZT23 and ZT43. **(F)** Achilles and tendon tissues were harvested at the day phase (ZT3, day) or night phase (ZT15, night) and labeled with ^{14}C proline for 1 h in the presence of exogenous L-ascorbate. Higher incorporation of ^{14}C was observed in the night phase. **(G)** Densitometry of ^{14}C-labeled collagen-I from western blot analysis showed significant increase in ^{14}C-labeled col-I in the night phase in both Achilles (n=5; *$p=0.0423$) and tail tendons (n=3; *$p=0.0395$). **(H)** Ratio of 14C-procollagen to total extracted collagen-I during 24 hours.

Figure 3. Rhythmic expression of genes regulating collagen trafficking from ER to Golgi

(A) Rhythmic expression of Sec61a2 mRNA and (**B**) Sec61a2 protein levels. **(C)** Images of electron microscopy of transverse sections across mouse tendons fibroblasts *in vivo* showing the endoplasmic reticulum (ER) at different time points. Bars 500 nm. **(D)** Quantification of ribosome docking onto ER show differences at ZT2 and ZT15.5 in tendon fibroblasts *in vivo* (***$p<0.001$). **(E)** Immunofluorescence analysis of synchronized MEFs showed that CRSISPR/Cas9-mediated KO of *Sec61a1* and *Sec61a2* prevented collagen-I fibre assembly in the extracellular matrix. **(F)** Immunofluorescence analysis of collagen-I entry into the ER (detected via the marker calnexin) showed little co-localization of collagen-I and calnexin in Sec61a1 and Sec61a2 KO MEFs compared to wild type MEFs. (**G**) Rhythmic expression of *Mia3* and (**H**) Tango1. **(I)** Immunofluorescence analysis showed collagen-I retention in the ER (detected via the marker protein disulfide isomerase (Pdi)) in cells with siRNA-mediated *Mia3* knock down (*Mia3* KD). Staining of

control cells showed collagen-I fibres in the extracellular matrix (white arrows). (**J**) Rhythmic expression of Pde4d and (**K**) Pde4d. **(L)** Immunofluorescence analysis of collagen chaperone Hsp47, and ERGIC and the cis-Golgi (detected by marker Gm130) in synchronized MEFs showed gradual co-localization of Hsp47 with Gm130 (see insets). **(M)** Immunofluorescence analysis of Hsp47 in siRNA-mediated Pde4d-depleted cells showed accumulation of Hsp47 in Gm130 compared to control MEFs. **(N)** Immunofluorescence analysis of collagen-I in cells treated with Cdp840, which blocks Pde4d transcription, showed collagen-I secretion was blocked and there was accumulation in the ER (Hsp47 marker). A control treatment of 1 mM DMOG also inhibited PC-I secretion but had no effect on Pde4d expression (see Fig. S3J). Transcripts were detected by microarray during a 48-h period (multiple probe sets are shown if present; n=2; bars show SEM). Protein was assessed during a 24-h period. Levels of Gapdh served as loading controls. CT, circadian time.

Figure 4. Circadian clock-regulated PC-I trafficking post Golgi

(**A**) Rhythmic expression of *Vps33b* and (**B**) Vps33b. NS, non-specific protein. Levels of Gapdh served as loading controls. CT, circadian time. (**C**) Immunofluorescence localization of col-I in control and Vps33b knockdown cells. Inserts show intracellular retention of collagen-I and absence of extracellular collagen fibres in Vps33b knockdown cells. (**D**) Quantitative PCR comparison of *Sec61a2*, *Mia3*, *Pde4d* and *Vps33b* in wild-type and *Clock*Δ*19* tendons sampled at ZT3 (*Sec61a2* **p<0.01, *Pde4d* *p<0.05) and ZT15 (*Sec61a2* **p<0.01, *Pde4d* **p<0.01, *Vps33b* **p<0.01). (**F**) Schematic representation of the points of control by the circadian step during the secretion of PC-I.

Supplementary Figure 1

(A) Luminometry recordings of endogenous circadian rhythms and re-initiation of the rhythms with dexamethasone (arrow) evident in dissected Achilles and tail tendons of wild type mice but not of Scx-Cre:*Bmal1* lox/lox mice bred on a *Per2*::Luciferase background. A residual rhythm observed in the Scx-Cre::*Bmal1* lox/lox tendons was likely due to cells that were not derived from Scleraxis-lineage cells. **(B)** Relative amplitude of wild type and Scx-Cre:*Bmal1* lox/lox tail and Achilles tendon circadian clocks at 6-weeks of age (n=5 tail tendons, n=4 Achilles tendons; *p<0.05, **p<0.001). **(C)** Scx-Cre:*Bmal1* lox/lox tendons are mechanically weaker (n=6; **p<0.01, ***p <0.001) and thicker (n=6; **p<0.01) than age-matched (6-weeks old) wild type mice. **(D)** *Clock*Δ*19* tendons are mechanically weaker (n=6; *p<0.05, **p<0.01) and thicker (n=6; **p<0.01) than age-matched (6-weeks old) wild type mice. **(E)** Fibril volume fraction is unchanged in *Clock*Δ*19* tendons compared to wild type tendons. **(F)** Elastic modulus of Achilles tendon is not time-of-day dependent (n=4). **(G)** Representative hysteresis curves from cyclic loading show energy loss is greater in tendons taken at ZT15. **(H)** Time constants derived from stress-relaxation from an initial 1 N load of Achilles tendon sampled at ZT3 compared to ZT15 (T_1, T_2 and T_3) (n=4; *p<0.05).

Supplementary Figure 2

Heatmap of Pearson correlation coefficients (*r*) for pairwise comparison of each sample, calculated from normalized peptide intensities. Each square represents a single comparison with intensity of color denoting *r* according to the color bar (right). High average and minimum *r* values denote high reproducibility between biological replicates.

Supplementary Figure 3

(A) Phosphorimager analysis of 1 h ^{14}C proline labeling of mouse Achilles tendon. Proteins were extracted into neutral buffer containing NP40 buffer extraction. Higher incorporation of 14C is observed in the night phase. (**B**) Western blot analysis of the samples shown in (A). Collagen-I was observed with an anti-collagen-I antibody. (**C**) Relative expression of *Sec61a1* and *Sec61a2* mRNA was reduced in MEFs after

CRISPR-Cas9-mediated deletion of both *Sec61a1* and *Sec61a2* compared to control wild type MEFs (n=3; *p<0.05, ***p<0.0001). (**D**) Western blot analysis of intracellular and conditioned media from MEFs treated with CRISPR-Cas9 showed that depletion of Sec61a2 inhibits collagen-I secretion (analysis of conditioned media). Levels of vinculin protein served as a loading control. **(E)** Relative expression of *Mia3* mRNA was reduced in MEFs treated with siRNA targeting *Mia3* compared to cells treated with scrambled control siRNA (n=3; ***p<0.0001). **(F)** Western blot analysis of MEFs treated with siRNA targeting Mia3. Levels of vinculin protein served as a loading control. **(G)** Western blot analysis of MEFs treated with siRNAs targeting *Pde4d* showed depletion of Pde4d protein. Levels of Gapdh protein served as a loading control. **(H)** Inhibition of *Pde4d* mRNA expression using the chemical inhibitor Cdp840 but not with DMOG. Levels of Gapdh mRNA served as a loading control. **(I)** Immunofluorescence analysis showed that Pde4d depletion in MEFs using siRNAs or Cdp840 blocked collagen-I secretion into the matrix, which was unaffected in control cells (white arrows). **(J)** Treatment of MEFs with Cdp840 or control DMOG caused collagen-I retention in the ER (Hsp47 marker), which was unaffected in control cells (white arrow). Bars 10 µm. **(K)** Immunofluorescence analysis of fibronectin showed that treatment with Cdp840 did not affect fibronectin secretion. **(L)** Relative expression of *Vps33b* mRNA in iTTFs clones after CRISPR-Cas9-mediated deletion of *Vps33b* (n=3; *p<0.05, ***p<0.001). **(M)** Western blot analysis of VPS33b protein from Vsp33b KO iTTF clones. Vinculin protein served as a loading control. **(N)** Relative expression of Vps33b mRNA in MEFs after CRISPR-Cas9-mediated deletion of Vps33b (n=3; ***p<0.001). Controls were wild type MEFs that underwent electroporation with Cas9 protein but no gRNA.

Supplementary Figure 4

Immunofluorescence analysis of synchronized iTTFs showed collagen-I secretion (white arrows) was inhibited in CRISPR-mediated Vps33b KO clones (C9 and D5), where collagen-I was retained in the ER (PDI marker). Increased retention of collagen-I occurs in the Golgi (Gm130 marker) when Vps33b was knocked out (see insets). White arrows indicate extracellular collagen fibres, which were depleted in Vsp33b KO cells. Red, col-I. Green, PDI.

Supplementary Data

MetaCycle output (columns A-X) for timed series LC-MS/MS analysis of proteins extracted from 6 week-old mouse male tail tendon (columns Y-AJ).

Supplementary Movie 1

Real-time bioluminescence microscopy of dissected Achilles tendon from wild type *Per2*::Luciferase mice.

Supplementary Movie 2

Real-time bioluminescence microscopy of dissected Achilles tendon from ScxCre::*Bmal1* lox/lox *Per2*::Luciferase mice. The brightness for the Scx-Cre:*Bmal1* lox/lox tendon recording was increased to enable visualization.

References

1. T. Roenneberg, M. Merrow, Circadian clocks - the fall and rise of physiology. *Nat Rev Mol Cell Biol* **6**, 965-971 (2005).
2. N. Cermakian, P. Sassone-Corsi, Multilevel regulation of the circadian clock. *Nat Rev Mol Cell Biol* **1**, 59-67 (2000).

3. D. A. Parry, A. S. Craig, Quantitative electron microscope observations of the collagen fibrils in rat-tail tendon. *Biopolymers* **16**, 1015-1031 (1977).
4. J. D. Humphries, A. Byron, M. J. Humphries, Integrin ligands at a glance. *J Cell Sci* **119**, 3901-3903 (2006).
5. S. A. Wickstrom, R. Fassler, Regulation of membrane traffic by integrin signaling. *Trends Cell Biol* **21**, 266-273 (2011).
6. R. T. Piszczatowski, N. H. Lents, Regulation of the CCN genes by vitamin D: A possible adjuvant therapy in the treatment of cancer and fibrosis. *Cell Signal* **28**, 1604-1613 (2016).
7. C. Y. Yeung *et al.*, Gremlin-2 is a BMP antagonist that is regulated by the circadian clock. *Sci Rep* **4**, 5183 (2014).
8. I. Raote *et al.*, TANGO1 builds a machine for collagen export by recruiting and spatially organizing COPII, tethers and membranes. *Elife* **7**, (2018).
9. E. A. Miller, R. Schekman, COPII - a flexible vesicle formation system. *Curr Opin Cell Biol* **25**, 420-427 (2013).
10. M. H. Vitaterna *et al.*, Mutagenesis and mapping of a mouse gene, Clock, essential for circadian behavior. *Science* **264**, 719-725 (1994).
11. T. Starborg *et al.*, Using transmission electron microscopy and 3View to determine collagen fibril size and three-dimensional organization. *Nat Protoc* **8**, 1433-1448 (2013).
12. M. K. Bunger *et al.*, Progressive arthropathy in mice with a targeted disruption of the Mop3/Bmal-1 locus. *Genesis* **41**, 122-132 (2005).
13. P. Janich, A. B. Arpat, V. Castelo-Szekely, M. Lopes, D. Gatfield, Ribosome profiling reveals the rhythmic liver translatome and circadian clock regulation by upstream open reading frames. *Genome Res* **25**, 1848-1859 (2015).
14. L. Stefanovic, L. Longo, Y. Zhang, B. Stefanovic, Characterization of binding of LARP6 to the 5' stem-loop of collagen mRNAs: implications for synthesis of type I collagen. *RNA Biol* **11**, 1386-1401 (2014).
15. T. A. Rapoport, B. Jungnickel, U. Kutay, Protein transport across the eukaryotic endoplasmic reticulum and bacterial inner membranes. *Annu Rev Biochem* **65**, 271-303 (1996).
16. E. Park, T. A. Rapoport, Mechanisms of Sec61/SecY-mediated protein translocation across membranes. *Annu Rev Biophys* **41**, 21-40 (2012).
17. S. Shao, R. S. Hegde, Membrane protein insertion at the endoplasmic reticulum. *Annu Rev Cell Dev Biol* **27**, 25-56 (2011).
18. B. Van den Berg *et al.*, X-ray structure of a protein-conducting channel. *Nature* **427**, 36-44 (2004).
19. K. Saito *et al.*, TANGO1 facilitates cargo loading at endoplasmic reticulum exit sites. *Cell* **136**, 891-902 (2009).
20. E. P. O'Brien, P. Ciryam, M. Vendruscolo, C. M. Dobson, Understanding the influence of codon translation rates on cotranslational protein folding. *Acc Chem Res* **47**, 1536-1544 (2014).
21. G. Zhang, Z. Ignatova, Folding at the birth of the nascent chain: coordinating translation with co-translational folding. *Curr Opin Struct Biol* **21**, 25-31 (2011).
22. Y. Ishikawa, S. Ito, K. Nagata, L. Y. Sakai, H. P. Bachinger, Intracellular mechanisms of molecular recognition and sorting for transport of large extracellular matrix molecules. *Proc Natl Acad Sci U S A* **113**, E6036-E6044 (2016).
23. N. Nagai *et al.*, Embryonic lethality of molecular chaperone hsp47 knockout mice is associated with defects in collagen biosynthesis. *J Cell Biol* **150**, 1499-1506 (2000).
24. T. Koide *et al.*, Specific recognition of the collagen triple helix by chaperone HSP47: minimal structural requirement and spatial molecular orientation. *J Biol Chem* **281**, 3432-3438 (2006).
25. T. Koide *et al.*, Specific recognition of the collagen triple helix by chaperone HSP47. II. The HSP47-binding structural motif in collagens and related proteins. *J Biol Chem* **281**, 11177-11185 (2006).
26. J. Cancino *et al.*, Control systems of membrane transport at the interface between the endoplasmic reticulum and the Golgi. *Dev Cell* **30**, 280-294 (2014).
27. B. Banushi *et al.*, Regulation of post-Golgi LH3 trafficking is essential for collagen homeostasis. *Nat Commun* **7**, 12111 (2016).

28. N. Verzijl *et al.*, Effect of collagen turnover on the accumulation of advanced glycation end products. *J Biol Chem* **275**, 39027-39031 (2000).
29. C. T. Thorpe *et al.*, Aspartic acid racemization and collagen degradation markers reveal an accumulation of damage in tendon collagen that is enhanced with aging. *J Biol Chem* **285**, 15674-15681 (2010).
30. K. M. Heinemeier *et al.*, Radiocarbon dating reveals minimal collagen turnover in both healthy and osteoarthritic human cartilage. *Sci Transl Med* **8**, 346ra390 (2016).
31. K. M. Heinemeier, P. Schjerling, J. Heinemeier, S. P. Magnusson, M. Kjaer, Lack of tissue renewal in human adult Achilles tendon is revealed by nuclear bomb (14)C. *FASEB J* **27**, 2074-2079 (2013).
32. S. S. Sivan *et al.*, Collagen turnover in normal and degenerate human intervertebral discs as determined by the racemization of aspartic acid. *J Biol Chem* **283**, 8796-8801 (2008).
33. K. Dideriksen *et al.*, Effect of acute exercise on patella tendon protein synthesis and gene expression. *Springerplus* **2**, 109 (2013).
34. T. A. Jarvinen *et al.*, Mechanical loading regulates tenascin-C expression in the osteotendinous junction. *J Cell Sci* **112 Pt 18**, 3157-3166 (1999).
35. S. Rosager *et al.*, Load-displacement properties of the human triceps surae aponeurosis and tendon in runners and non-runners. *Scand J Med Sci Sports* **12**, 90-98 (2002).
36. H. L. Birch, L. McLaughlin, R. K. Smith, A. E. Goodship, Treadmill exercise-induced tendon hypertrophy: assessment of tendons with different mechanical functions. *Equine Vet J Suppl*, 222-226 (1999).
37. S. L. Woo *et al.*, The biomechanical and biochemical properties of swine tendons--long term effects of exercise on the digital extensors. *Connect Tissue Res* **7**, 177-183 (1980).
38. H. Langberg, L. Rosendal, M. Kjaer, Training-induced changes in peritendinous type I collagen turnover determined by microdialysis in humans. *J Physiol* **534**, 297-302 (2001).
39. H. Langberg, D. Skovgaard, L. J. Petersen, J. Bulow, M. Kjaer, Type I collagen synthesis and degradation in peritendinous tissue after exercise determined by microdialysis in humans. *J Physiol* **521 Pt 1**, 299-306 (1999).
40. A. Blumsohn *et al.*, The effect of calcium supplementation on the circadian rhythm of bone resorption. *J Clin Endocrinol Metab* **79**, 730-735 (1994).
41. B. J. Pedersen, A. Schlemmer, C. Rosenquist, C. Hassager, C. Christiansen, Circadian rhythm in type I collagen formation in postmenopausal women with and without osteopenia. *Osteoporos Int* **5**, 472-477 (1995).
42. A. M. Bollen, M. D. Martin, B. G. Leroux, D. R. Eyre, Circadian variation in urinary excretion of bone collagen cross-links. *J Bone Miner Res* **10**, 1885-1890 (1995).
43. V. Everts, E. van der Zee, L. Creemers, W. Beertsen, Phagocytosis and intracellular digestion of collagen, its role in turnover and remodelling. *Histochem J* **28**, 229-245 (1996).
44. V. Everts *et al.*, Cathepsin K deficiency in pycnodysostosis results in accumulation of non-digested phagocytosed collagen in fibroblasts. *Calcif Tissue Int* **73**, 380-386 (2003).
45. E. Blitz, A. Sharir, H. Akiyama, E. Zelzer, Tendon-bone attachment unit is formed modularly by a distinct pool of Scx- and Sox9-positive progenitors. *Development* **140**, 2680-2690 (2013).
46. K. F. Storch *et al.*, Intrinsic circadian clock of the mammalian retina: importance for retinal processing of visual information. *Cell* **130**, 730-741 (2007).
47. S. H. Yoo *et al.*, PERIOD2::LUCIFERASE real-time reporting of circadian dynamics reveals persistent circadian oscillations in mouse peripheral tissues. *Proc Natl Acad Sci U S A* **101**, 5339-5346 (2004).
48. N. S. Kalson *et al.*, An experimental model for studying the biomechanics of embryonic tendon: Evidence that the development of mechanical properties depends on the actinomyosin machinery. *Matrix Biol* **29**, 678-689 (2010).
49. D. B. Bekker-Jensen *et al.*, An Optimized Shotgun Strategy for the Rapid Generation of Comprehensive Human Proteomes. *Cell systems* **4**, 587-599 e584 (2017).
50. L. J. Goeminne, K. Gevaert, L. Clement, Peptide-level Robust Ridge Regression Improves Estimation, Sensitivity, and Specificity in Data-dependent Quantitative Label-free Shotgun Proteomics. *Mol Cell Proteomics* **15**, 657-668 (2016).

51. S. Tyanova *et al.*, The Perseus computational platform for comprehensive analysis of (prote)omics data. *Nature methods* **13**, 731-740 (2016).
52. P. J. Huber, Robust Estimation of a Location Parameter. *Ann. Math. Statist.* **35**, 73-101 (1964).
53. K. Kammers, R. N. Cole, C. Tiengwe, I. Ruczinski, Detecting Significant Changes in Protein Abundance. *EuPA open proteomics* **7**, 11-19 (2015).
54. G. K. Smyth, Linear models and empirical bayes methods for assessing differential expression in microarray experiments. *Statistical applications in genetics and molecular biology* **3**, Article3 (2004).
55. Y. Benjamini, H. Y., Controlling the False Discovery Rate: A Practical and Powerful Approach to Multiple Testing. *Journal of the Royal Statistical Society. Series B (Methodological)* **57**, 289-300 (1995).
56. G. Wu, R. C. Anafi, M. E. Hughes, K. Kornacker, J. B. Hogenesch, MetaCycle: an integrated R package to evaluate periodicity in large scale data. *Bioinformatics* **32**, 3351-3353 (2016).
57. R. Ihaka, R. Gentleman, R: A Language for Data Analysis and Graphics. *Journal of Computational and Graphical Statistics* **5**, 299-314 (1996).
58. C. Y. Yeung *et al.*, Chick tendon fibroblast transcriptome and shape depend on whether the cell has made its own collagen matrix. *Sci Rep* **5**, 13555 (2015).
59. M. B. Alvarez *et al.*, Immortalization and characterization of osteoblast cell lines generated from wild-type and Nmp4-null mouse bone marrow stromal cells using murine telomerase reverse transcriptase (mTERT). *J Cell Physiol* **227**, 1873-1882 (2012).
60. K. J. Livak, T. D. Schmittgen, Analysis of relative gene expression data using real-time quantitative PCR and the 2(-Delta Delta C(T)) Method. *Methods* **25**, 402-408 (2001).

Yeung, Garva et al. – Figure 1

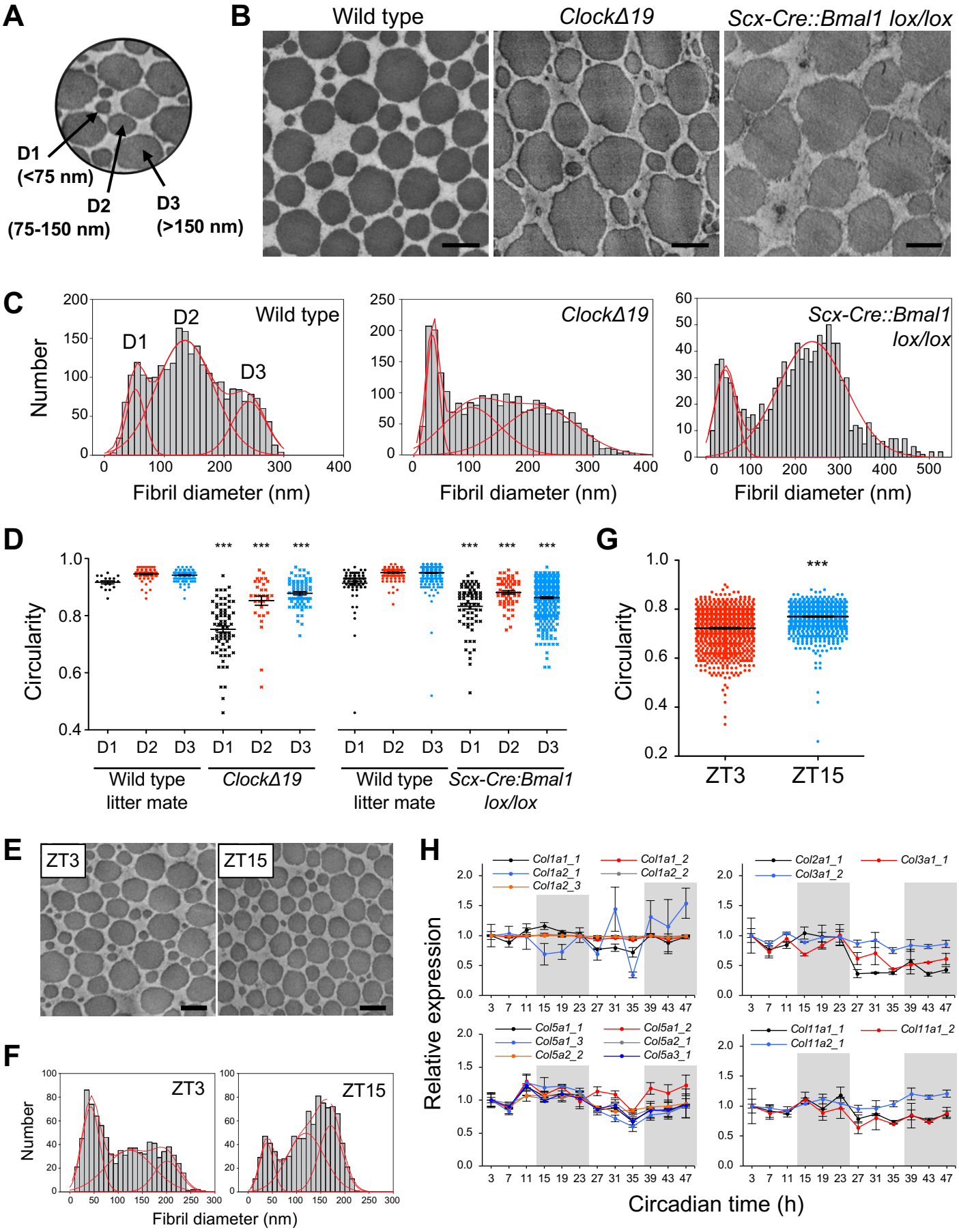

Yeung, Garva et al. – Figure 2

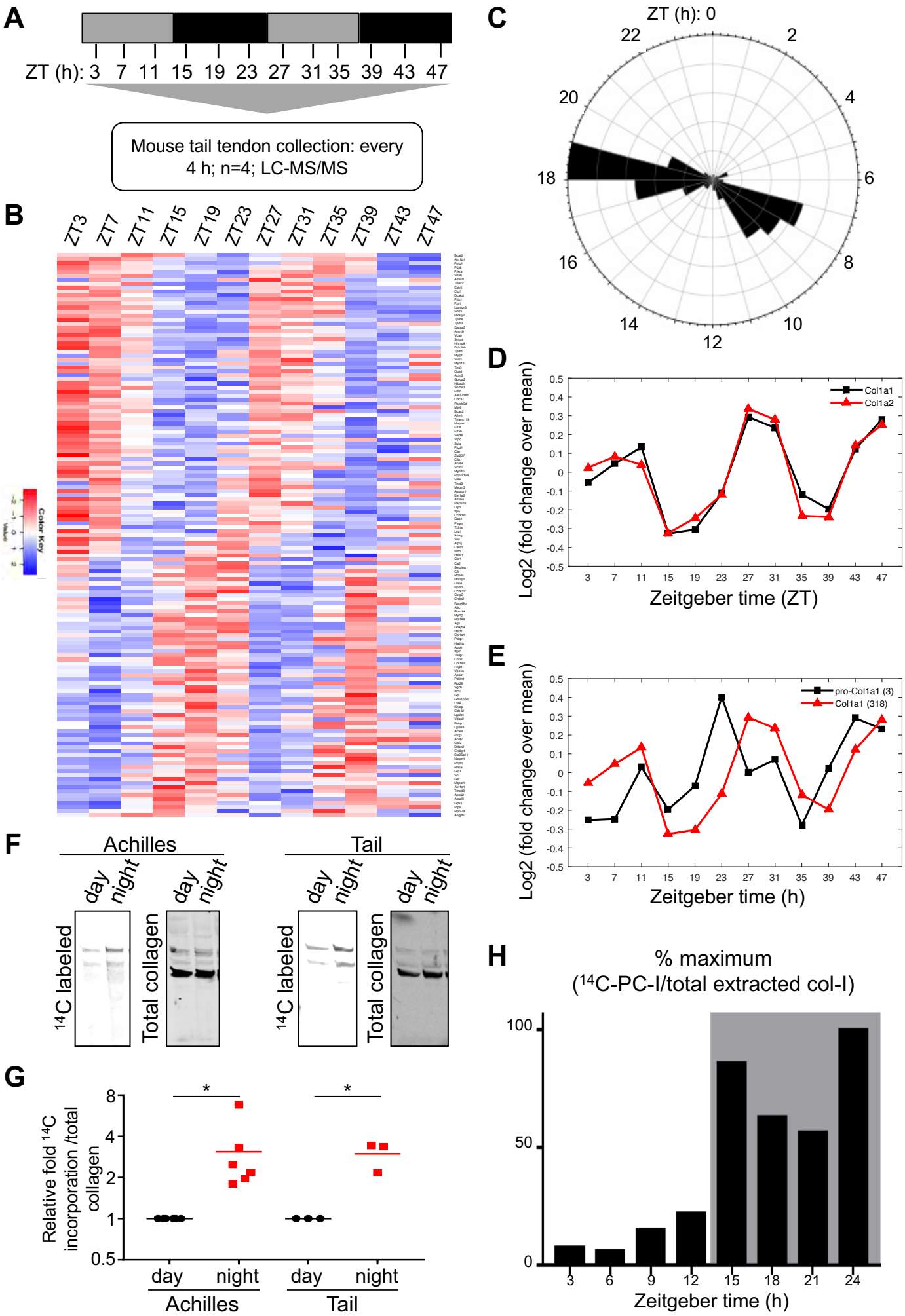

Yeung, Garva et al. – Figure 3

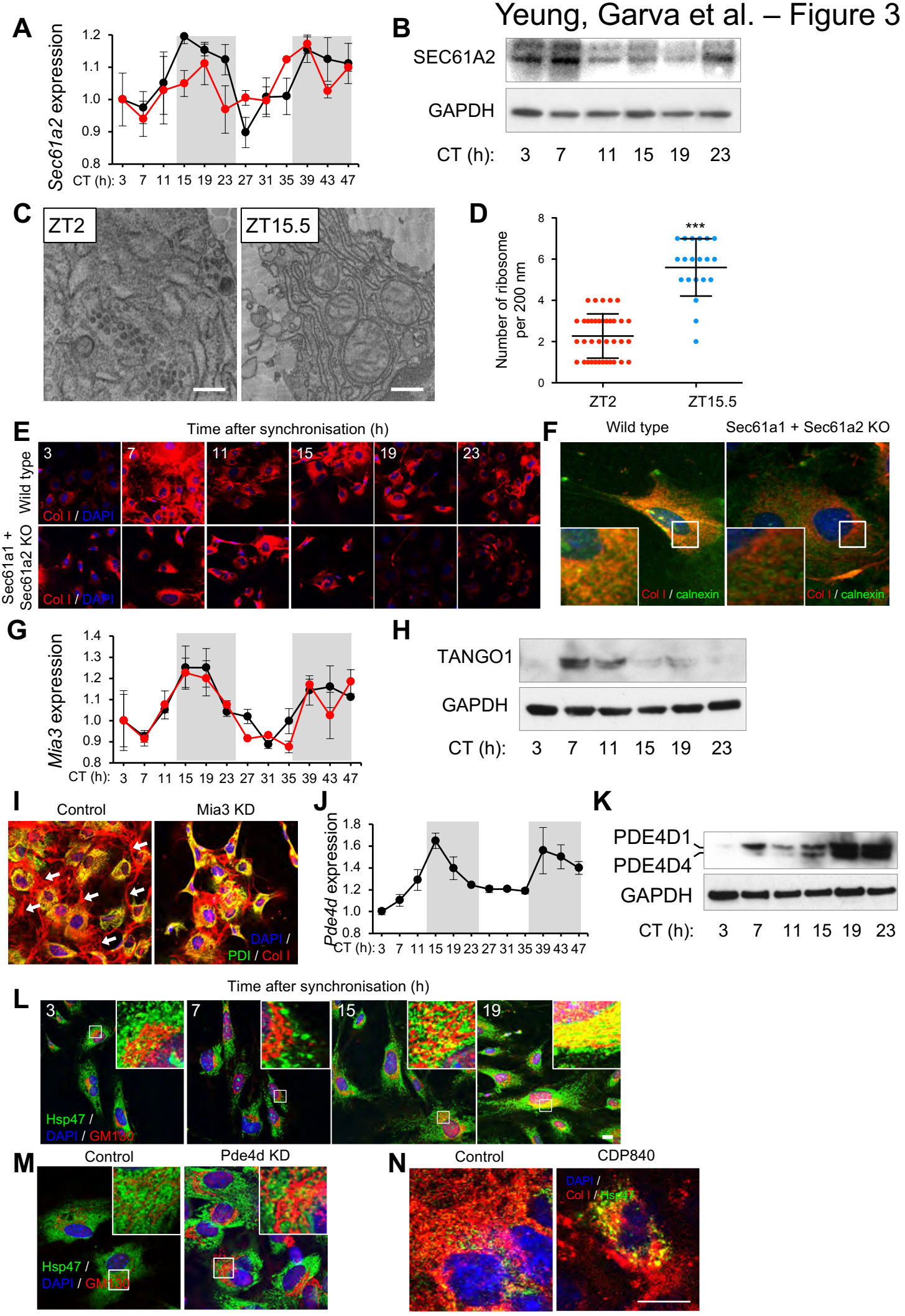

Yeung, Garva et al. – Figure 4

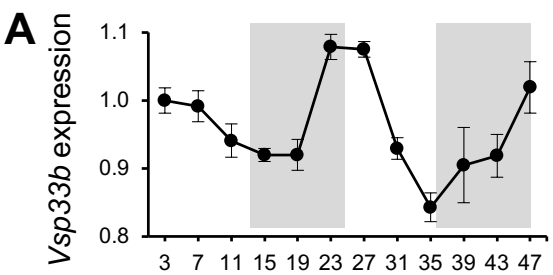

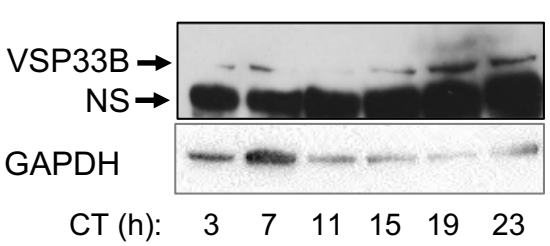

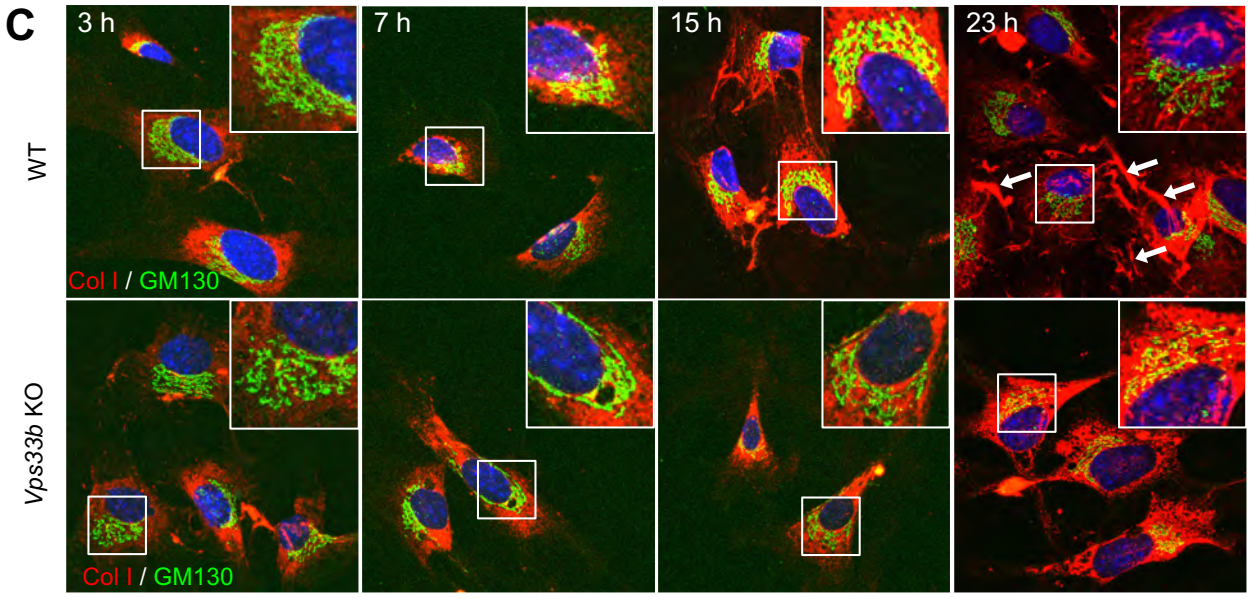

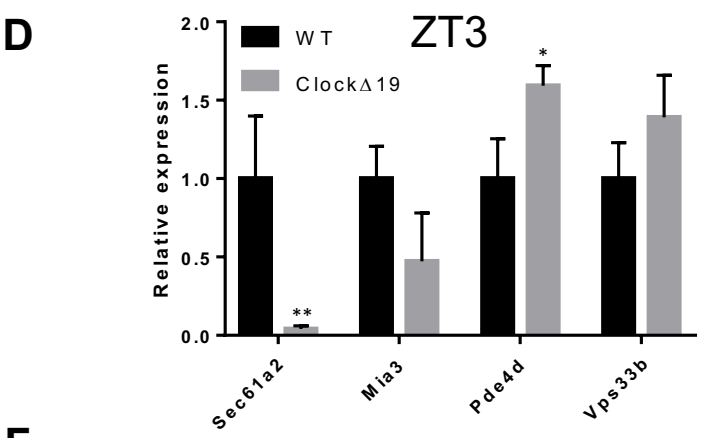

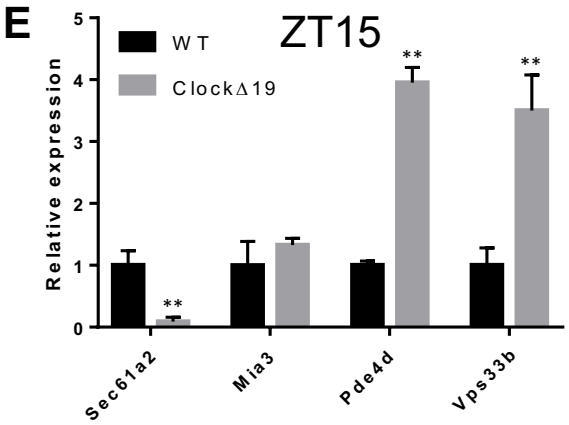

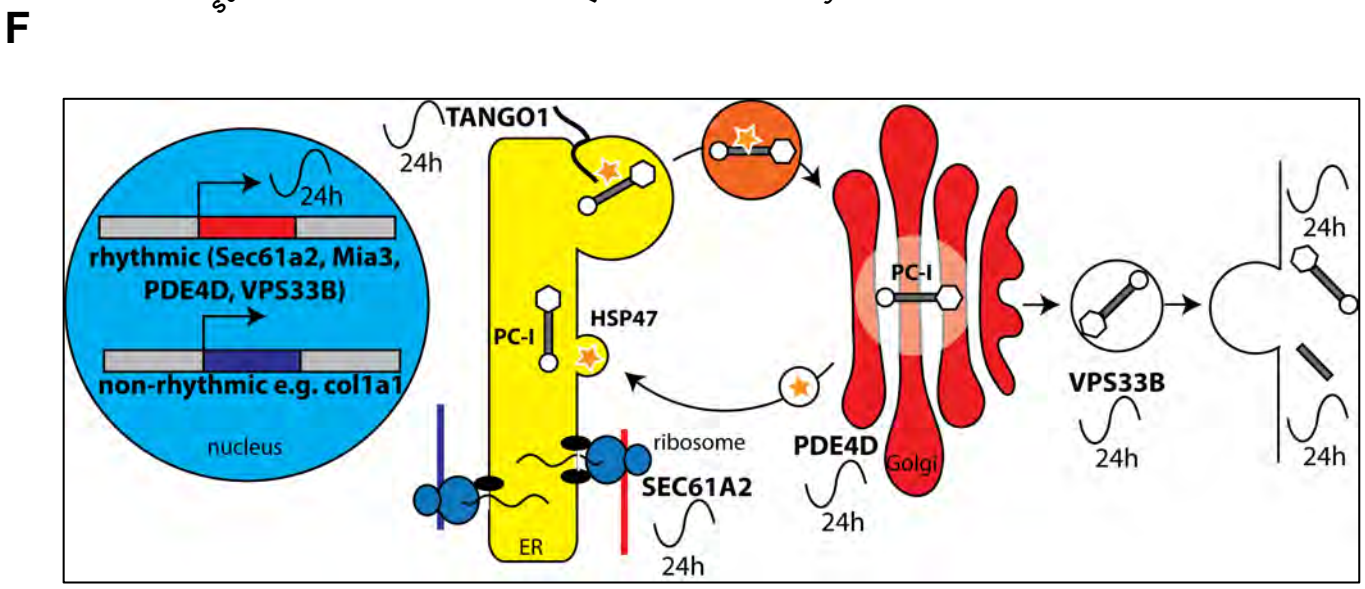

Yeung, Garva et al. – Figure S1

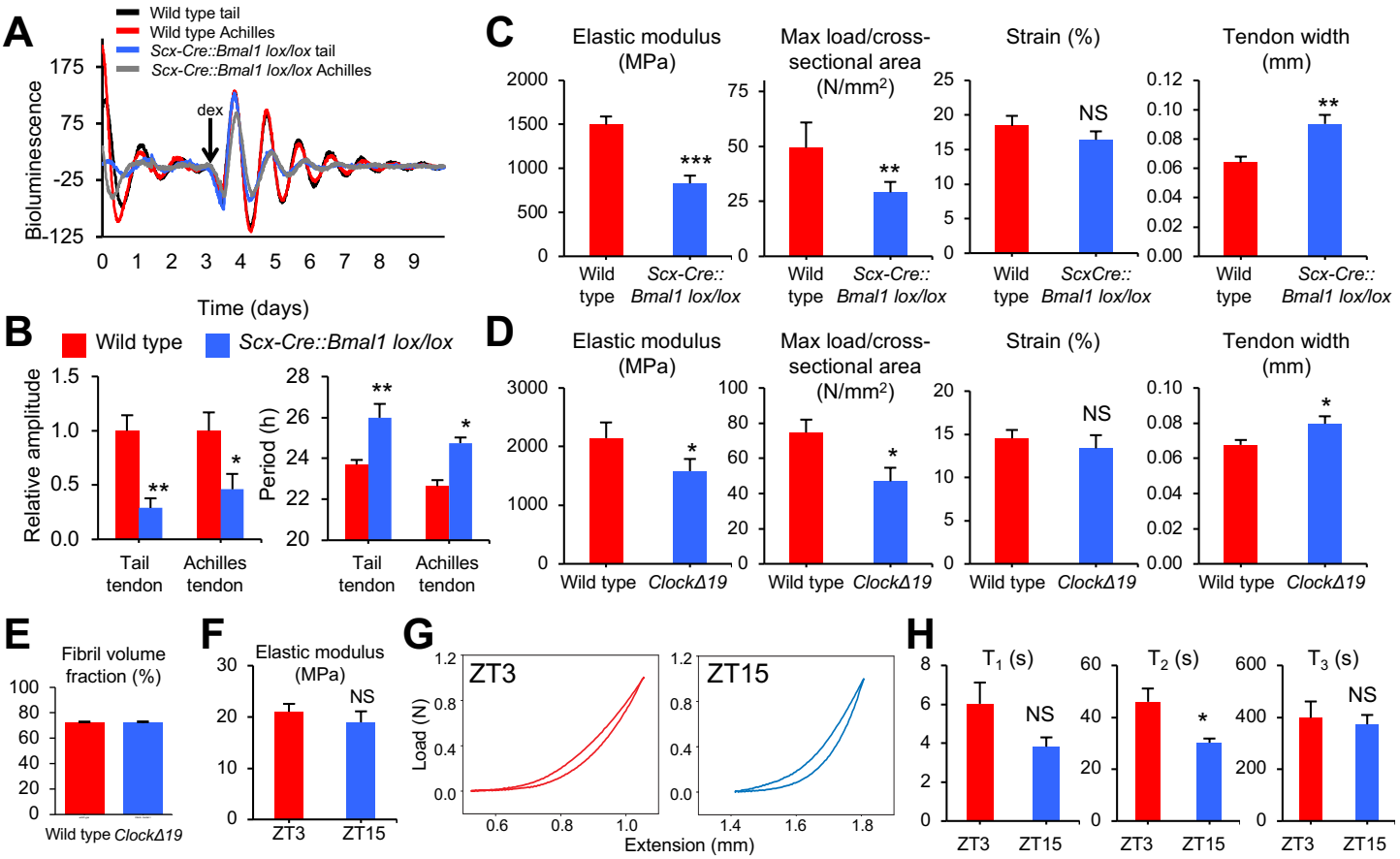

Yeung, Garva et al. – Figure S2

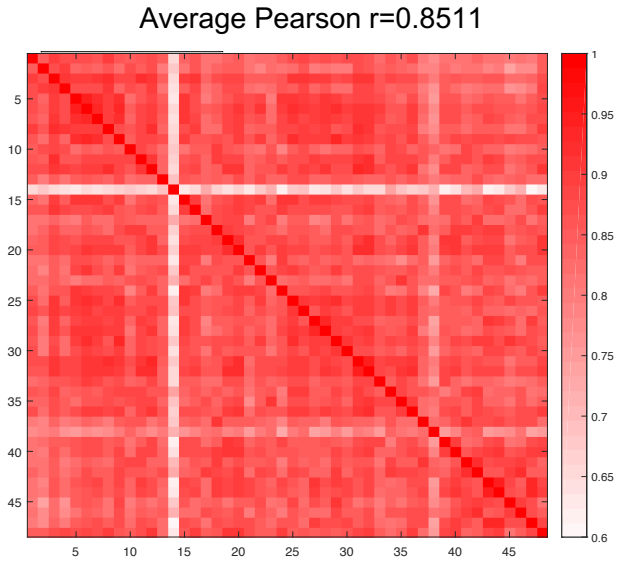

Yeung, Garva et al. – Figure S3

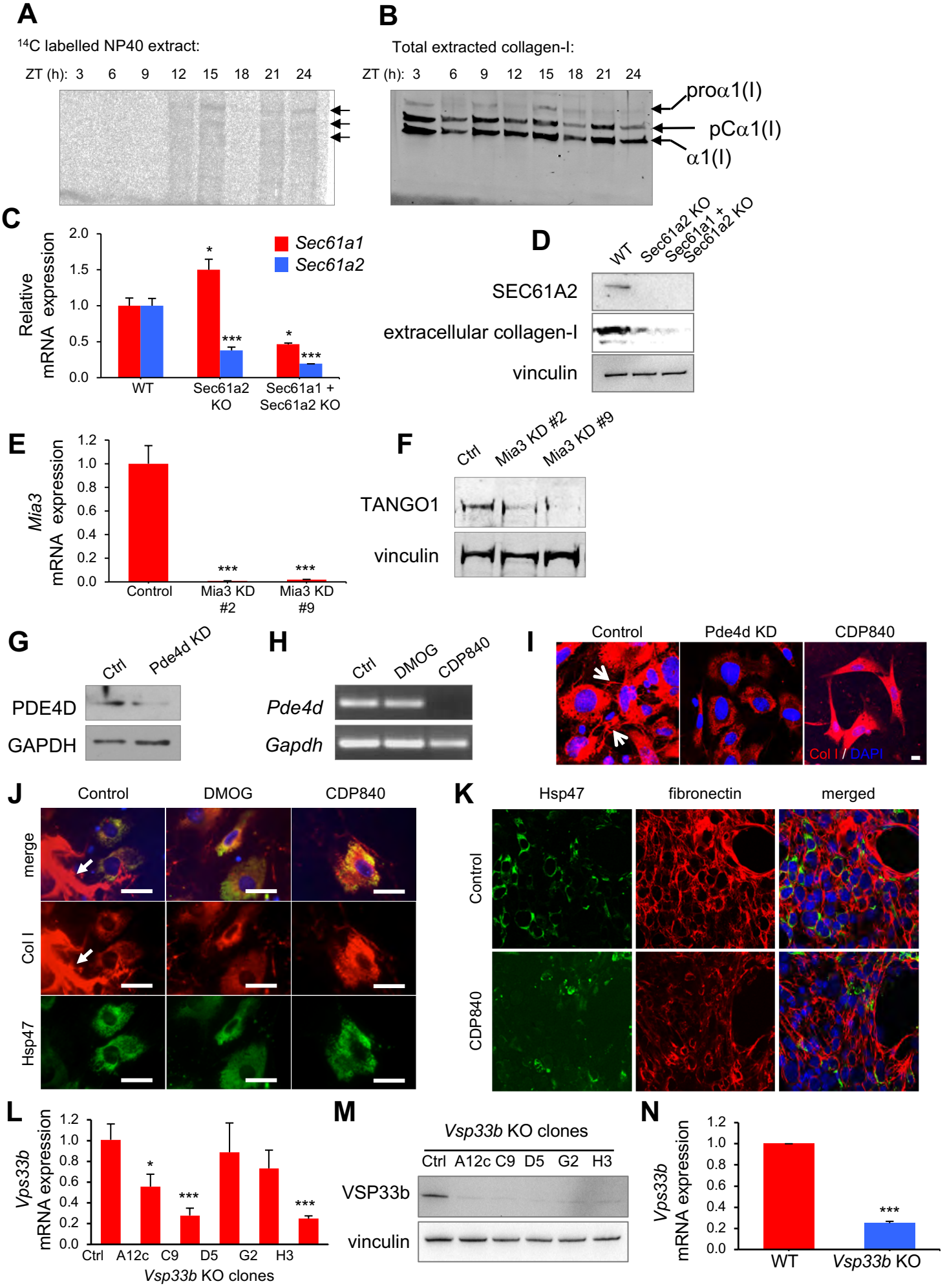
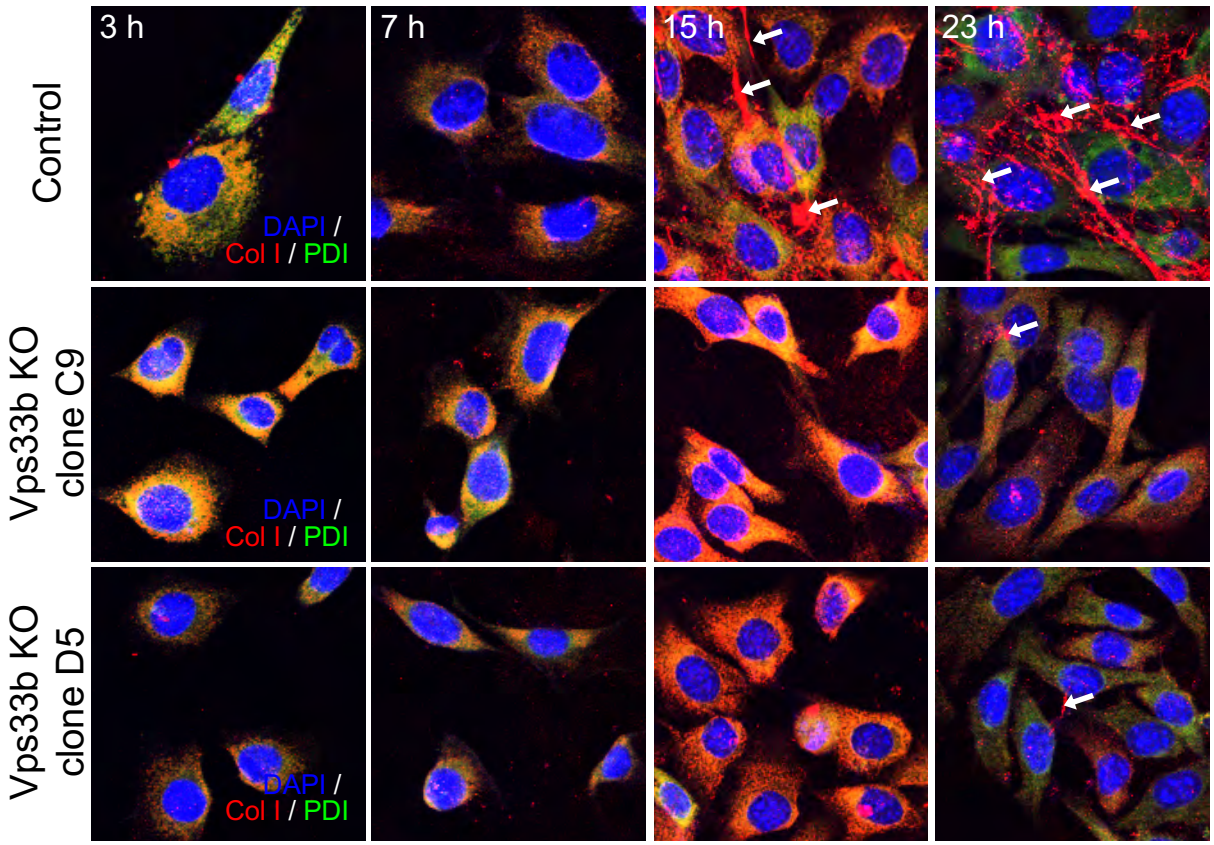
Yeung, Garva et al. – Figure S4